SANDIA REPORT

Three-Dimensional Wind Simulation

Paul S. Veers

SF2900Q(8-81)

Three-Dimensional Wind Simulation

Paul S. Veers
Applied Mechanics Division IV
Sandia National Laboratories
Albuquerque, New Mexico 87185

Abstract

A method for numerically simulating a three-dimensional field of turbulent wind-speed (the "Sandia method") for use in the aerodynamic and structural analyses of wind turbines is presented. The required inputs are single point power spectral densities (PSDs) and the coherence function. Suggestions for appropriate inputs and an example calculation are included. The simulation method is used to obtain "rotationally sampled" PSDs, which are compared with measurements obtained by Pacific Northwest Laboratories. The results show that the Sandia method is capable of producing simulations that agree with the measurements, especially when the coherence function is augmented from the usual form to include the ratio of spatial separation over height raised to the 0.25 power. The method is specialized for horizontal axis wind turbine analysis by phase lagging the simulations at each point in space so that wind speeds are simulated only when the turbine blade passes the point, reducing storage requirements and computation time by about an order of magnitude. For vertical axis applications, where interpolation will be required, the error induced by the interpolation is estimated and eliminated by the addition of white noise.

Acknowledgements

Contents

1. Introduction

Wind simulation has become an important part of both vertical and horizontal axis wind turbine structural analysis. Because of the highly nonlinear relationship between atmospheric turbulence and aerodynamic loads on wind turbine blades, there continues to be interest in numerically simulating the winds and then calculating time series of blade loads. For mid-to-large size wind turbines, spatial variations in the turbulence must be considered and three-dimensional wind simulation is required.

The basic approach of the *Sandia method* [1] is to simulate wind-speed time series at several points in a plane perpendicular to the mean wind direction and to propagate the time series in the mean wind direction at the mean wind speed (i.e., using Taylor's frozen turbulence hypothesis). This is a "full-field" method in that it completely fills a three-dimensional block of space with a grid of instantaneous wind speeds. This is especially useful for VAWT applications where the blades sweep back and forth through the turbulence as it propagates through the rotor. Even one-dimensional turbulence inputs have been shown to produce some unexpected aerodynamic effects on VAWT loads [2]. Each point on a HAWT blade follows a simpler path tracing a circle in a vertical plane. An improvement to the Sandia method is obtained (for HAWT applications) by specializing the simulation for the points in space and time occupied by rotating HAWT blades.

The Sandia method for full field wind simulation has already been applied to both HAWT [3,4] and VAWT [5,6] structural analysis. Very little computer time is needed to produce a full field of simulated winds. The limiting factor is the rather hefty storage requirement. To simulate a time series of length M at N points in space requires more than $M(N^2 + N)/2$ storage locations. For HAWT applications, this storage requirement can be significantly reduced by using the efficient simulation technique described in this report.

The required input includes the single point turbulence PSDs for all N points and the coherence function, which describes how turbulence is correlated as a function of spatial separation, mean wind speed, and frequency. The coherence is assumed to be isotropic in the cross-wind plane and the cross spectral densities are assumed to be real valued. Neither of these assumptions are *necessary* for the method to work, but they both simplify implementation and are consistent with current knowledge of turbulence statistics. If improved turbulence descriptions are found, they could be included with minor modifications.

2. Review of the Simulation Method

The three-dimensional wind simulation method described in Ref. 1 and reviewed in this section is based on a method developed by Shinozuka [7] and more clearly outlined by Smallwood [8]. It creates N correlated time series based on the spectral matrix, $\mathbf{S}$. The diagonals of $\mathbf{S}$ are the power spectral densities (PSDs). Each off-diagonal term, S_{jk}, is the cross spectral density between points j and k.

For the purpose of numerical simulation, a discrete representation of each element in the spectral matrix is required. The continuous, one-sided PSD at point j, $G_{jj}(f)$, is discretized by dividing it into frequency bands Δf Hertz wide with the center frequency of each band designated as f_m. The correct variance is maintained by letting $S_{jj}(f_m) = G_{jj}(f_m)\Delta f/2$. [1] Each entry in the spectral matrix must contain $M/2$ frequency components to get a time series of length M using an FFT.

The magnitude of the cross spectrum between points j and k can be defined in terms of the PSDs and the coherence function, Coh_{jk}, by

$$|S_{jk}(f_m)| = Coh_{jk}(f_m, \Delta r_{jk}, U_{jk})\sqrt{S_{jj}(f_m)S_{kk}(f_m)} \qquad (2.1)$$

where the coherence is a function of frequency (f_m), distance between points j and k (Δr_{jk}), and mean wind speed at points j and k (U_{jk}). By assuming that there is an average phase of zero between any two points, the imaginary parts of the cross spectra are zero. Thus, the entire spectral matrix is defined by the PSDs and the coherence.

The N correlated time series are generated by linear combinations of N independent, white-noise processes. In this case, $\mathbf{S}$ can be written as the product of a transformation matrix, $\mathbf{H}$, and the transpose of its complex conjugate [7].

$$\mathbf{S}(f_m) = \mathbf{H}(f_m)\mathbf{H}^{*T}(f_m) \qquad (2.2)$$

where each entry in $\mathbf{S}$ and $\mathbf{H}$ is a function of frequency.

Because $\mathbf{S}$ is real, $\mathbf{H}$ must also be real and $\mathbf{H} = \mathbf{H}^*$. Because $\mathbf{S}$ is symmetric, it contains $(N^2 + N)/2$ independent entries while the full $\mathbf{H}$ contains N^2 entries; $\mathbf{H}$ is therefore not uniquely defined. If $\mathbf{H}$ is assumed to be lower triangular, however, the

---

[1] $S_{jj}(f_m)$ is the two-sided Fourier amplitude of the f_m^{th} frequency component. The normalization factor (1/2 in this case) must be unity if your FFT routine assumes a one-sided input.

nonzero entries will be uniquely defined and can be determined by a simple recursive set of equations:

$$H_{11} = S_{11}^{1/2}$$
$$H_{21} = S_{21}/H_{11}$$
$$H_{22} = (S_{22} - H_{21}^2)^{1/2}$$
$$H_{31} = S_{31}/H_{11}$$
$$\vdots$$
$$H_{jk} = \left(S_{jk} - \sum_{l=1}^{k-1} H_{jl}H_{kl} \right) / H_{kk}$$
$$H_{kk} = \left(S_{kk} - \sum_{l=1}^{k-1} H_{kl}^2 \right)^{1/2}$$

(2.3)

The elements of the $\mathbf{H}$ matrix can be thought of as the weighting factors for the linear combination of N independent, unit-magnitude, white-noise inputs that will yield N correlated outputs with the correct spectral matrix. Each row of $\mathbf{H}$ gives the contributions of all the inputs to the output at point k. Each column gives the contributions of the jth input to all of the outputs.

The independent, unit-magnitude, white-noise inputs are contained in an $N \times N$ diagonal matrix $\mathbf{X}$ such that

$$X_{jk}(f_m) = \begin{cases} e^{i\theta_{km}} & j = k \\ 0 & j \neq k \end{cases}$$

(2.4)

where i is $\sqrt{-1}$ and θ_{km} is the phase angle associated with the kth input point and the mth frequency component. θ_{km} is a uniformly distributed random variable on the interval $(0, 2\pi)$. This insures that the time series will approach a Gaussian process as the number of frequency components becomes large.

The matrix equation for the $N \times 1$ vector of complex Fourier coefficients of the simulated wind speed, $\mathbf{V}$, is given by

$$\mathbf{V} = \mathbf{H}\,\mathbf{X}\,\mathbf{1}$$

(2.5)

where $\mathbf{1}$ is an $N \times 1$ vector of ones.

The operations may be more easily visualized in summation notation where it is evident that the vector $\mathbf{1}$ is only present for the purpose of summing across each row of $\mathbf{HX}$.

$$V_j(f_m) = \sum_{k=1}^{j} H_{jk}(f_m)X_{kk}(f_m) = \sum_{k=1}^{j} H_{jk}(f_m)\, e^{i\theta_{km}}$$

(2.6)

Because $\mathbf{X}$ has all unit magnitude entries, the only effect it has is to apply a random phase to each column of $\mathbf{H}$. The summation form shows that the V_j depend

4

on the inputs from all the earlier points ($k \leq j$), which are weighted by the H_{jk}. The fact that each output does not depend on *all* the inputs is an artifact of selecting a lower triangular form for **H**. Assuming that **H** has other forms (e.g., symmetric) could eliminate the order dependence, but would also eliminate the simple recursive method of solving for the elements of **H**. A small example is shown in Appendix A to help illustrate how the above method works in practice.

The time series are obtained by taking the inverse Fourier transform of each element of **V**, resulting in a simulated wind speed at every time step for all N points in space. While this "full-field" representation may be necessary for VAWT applications, it produces many unused data for HAWT applications. Section 6 outlines how these extra data can be eliminated for the rotational sampling employed in HAWT applications.

3. Turbulence Power Spectral Densities (PSDs)

The basic input to any method of three-dimensional turbulence simulation is the wind speed PSD. Many models of turbulence PSDs have been proposed, starting with von Karman in 1948 [9]. Reference 1 used the PSD suggested by Frost [10] while Powell and Connell [11] suggest (rightly) that the Kaimal spectrum [12] is a more accurate representation. The Frost $(G_F(f))$, Kaimal $(G_K(f))$, and von Karman $(G_V(f))$ models are shown in Fig. 3.1, in the traditional form of logarithmic spectra $(fG(f)$ vs f, where f is the frequency in Hz). The formulas for these PSDs are:

$$G_F(f) = \frac{12.3U_{10}z[\ln((10/z_0)+1)\ln((z/z_0)+1)]^{-1}}{1 + 192[(fz/U_{10})\ln((10/z_0)+1)/\ln((z/z_0)+1)]^{\frac{5}{3}}} \qquad (3.1)$$

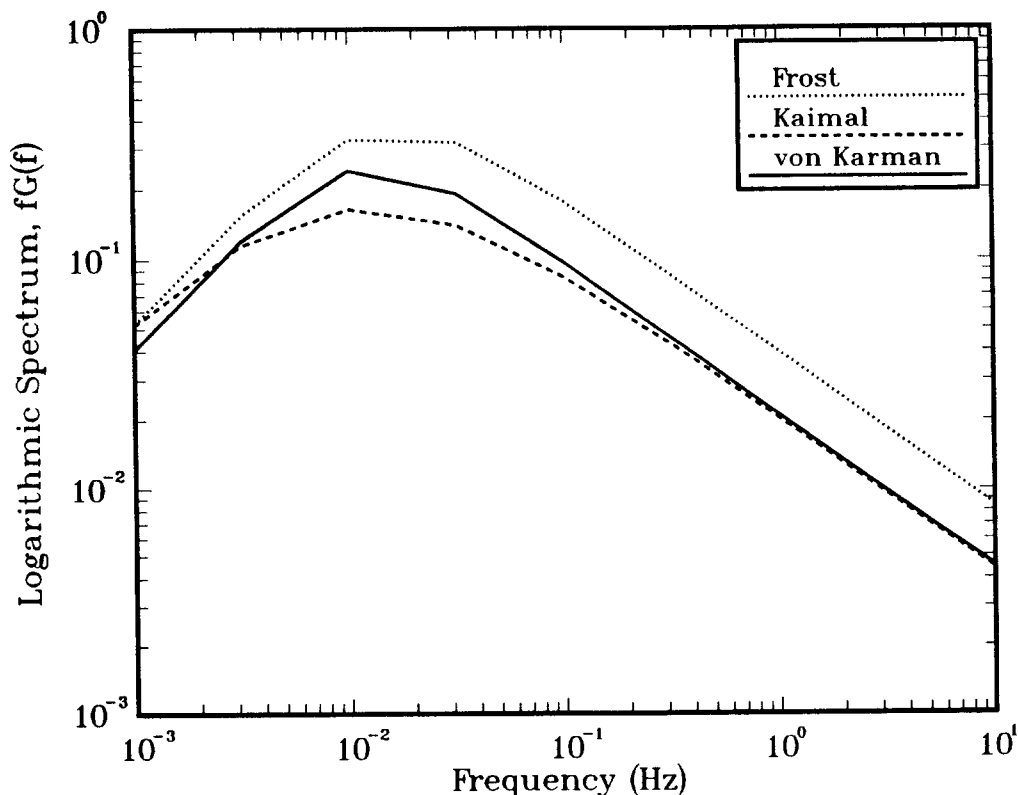$$G_K(f) = \frac{105u_*^2z/U}{(1 + 33(fz/U))^{\frac{5}{3}}} \qquad (3.2)$$

Figure 3.1. Turbulence PSD models by Frost [10], Kaimal [12], and von Karman [9] for $z_0 = .01m$, $L_x = 120m$, $U_{10} = 8m/s$, and $z = 30m$.

$$G_V(f) = \frac{4(5.7u_*^2)L_x/U}{1.339(1 + 39.48(fL_x/U)^2)^{\frac{5}{6}}} \tag{3.3}$$

where:

f is the frequency in Hertz

z is the height above ground in meters

z_0 is the surface roughness coefficient in meters

U_{10} is the mean wind speed in m/s at a height of 10 meters

U is the mean wind speed in m/s at a height of z meters

L_x is the integral length scale

u_* is the shear velocity, $u_* = \frac{0.4U}{\ln(z/z_0)}$

(The shear velocity is related to the turbulence variance, σ_u^2, in the von Karman spectrum by $\sigma_u^2 \approx 5.7u_*^2$.)

Figure 3.1 shows that all three PSDs have the same slope in the *inertial subrange* (high frequency). The Frost spectrum is significantly different than the other two because it is derived from the Kaimal spectrum with a *stable* atmosphere while the others apply to *neutral* atmospheres. The Kaimal and von Karman spectra are quite similar except that the Kaimal spectrum is slightly lower in the important region below one Hertz and, therefore, results in a turbulence intensity about 15% lower than the von Karman spectrum, for the parameter values used in Ref. 11 ($z_0 = .01m$, $L_x = 120m$, $U_{10} = 8m/s$, and $z = 30m$). These values result in different variances for all three PSDs, as shown in Fig. 3.1.

A recent review of the wind turbulence literature by Solari [13] highlights the uncertainty in determining the coefficients of any PSD model of atmospheric turbulence. Solari suggests that a deterministic representation for the turbulence PSD is *illusory*. He suggests that the basic form of the von Karman and Kaimal PSDs be retained, but that the parameter of the PSD be a random variable. Solari's PSD ($G_S(f)$) is of the form

$$G_S(f) = \frac{2.21u_*^2\beta^{2.5}z/U}{(1 + 3.31(f\beta^{1.5}z/U))^{\frac{5}{3}}} \tag{3.4}$$

where

$$\beta = \beta_m + \mu_\beta\Delta\beta$$

in which

$$\beta_m = \begin{cases} 7.5 & z_0 \leq 0.03 \\ 4.5 - 0.856\ln(z_0) & 0.03 \leq z_0 \leq 1.0 \\ 4.5 & 1.0 \leq z_0 \end{cases}$$

$$\Delta\beta = \begin{cases} 2.5 & z_0 \leq 0.03 \\ 2.0 - 0.143\ln(z_0) & 0.03 \leq z_0 \leq 1.0 \\ 2.0 & 1.0 \leq z_0 \end{cases}$$

7
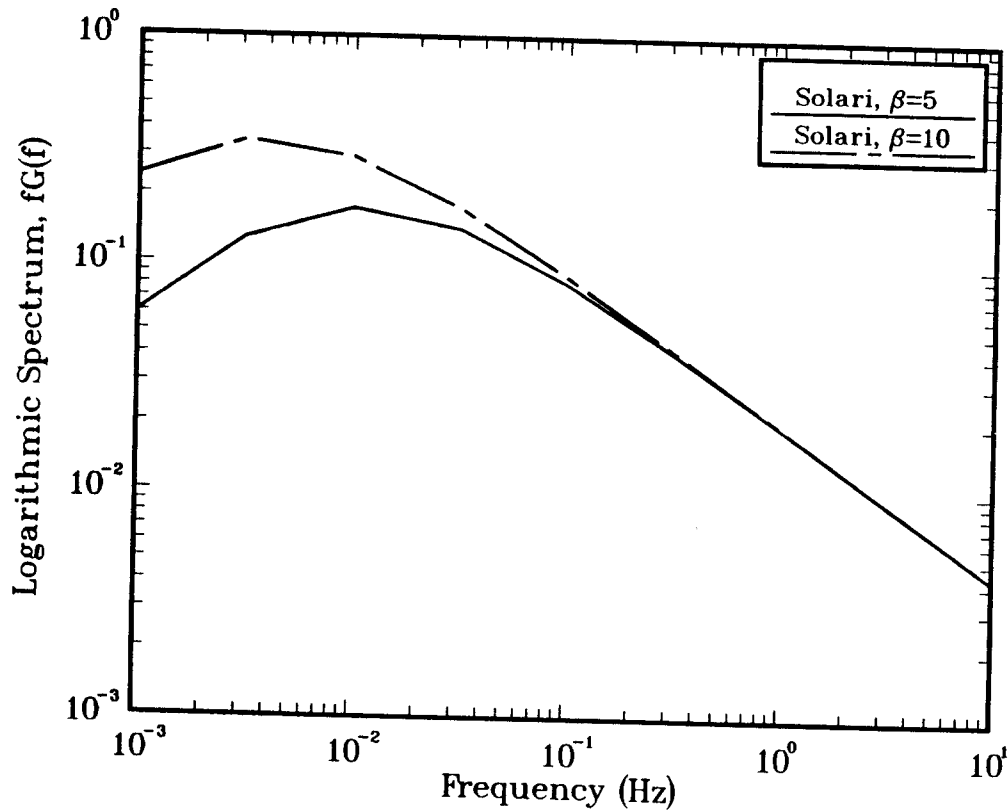
Figure 3.2. Turbulence PSDs by Solari [13] with the minimum and maximum values of the random variable β.

and μ_β is a uniformly distributed random variable on the interval (-1,1).

When β is varied in this way, it represents the scatter that is found in measured turbulence spectra. The two extremes of the Solari PSD are shown in Fig. 3.2 for the case of $z_0 \leq 0.03$. The variance of the turbulence, σ_u^2, is roughly βu_*^2. It may be argued that a uniform distribution on μ_β is artificial; one simple improvement would be to preserve the mean and standard deviation while substituting a continuous, one-sided distribution (e.g., Weibull). The important change is that β, and therefore the low frequency part of the PSD, is a random variable. The high frequency part matches both the von Karman and Kaimal PSDs.

8

4. Coherence

The coherence function is a frequency dependent measure of the amount of correlation between the wind speeds at two points in space. The usual form of the coherence function is exponential; the one given by Frost [10] (and previously suggested for use in the Sandia method [1]) is

$$Coh_{jk} = \exp\left(-\frac{C\Delta r_{jk}f}{U}\right) \qquad (4.1)$$

where Δr_{jk} is the distance (in meters) between points j and k.

The constant, C, (called the *coherence decrement*) has been estimated often for cross-wind separations without much agreement on any single value. Solari reports values ranging from 2 to 27 (Frost suggested $C = 7.5$ for lateral spacing) with the larger values of C tending to be associated with larger ratios of $\Delta r/z$, which suggests that the exponential form may not be capable of representing the full range of possible spacings of points. The form suggested by Solari is the same as Eq. 4.1 except that $U = U_{jk}$ is defined as the average of the mean wind speeds at points j and k (a minor revision) and that $C = C_{jk}$ is a function of the spacing between points, Δr_{jk}, and the mean height of the two points, $z_m = (z_j + z_k)/2$, given by

$$C_{jk} = b\left(\frac{\Delta r_{jk}}{z_m}\right)^{0.25} \qquad (4.2)$$

in which

$$b = 12 + 5\mu_b$$

As in the case of the spectral density, the coherence decrement is modeled as a random variable by defining μ_b to be uniformly distributed on the interval (-1,1).

The most important change is that the coherence function has been augmented by the dimensionless parameter $(\Delta r/z_m)^{0.25}$, thereby increasing the coherence when $(\Delta r/z_m) < 1$ and decreasing the coherence at greater spacings, as shown in Fig. 4.1 for four different frequencies. The selection of the 0.25 exponent in Eq. 4.2 provides a good fit to the data, but seems to be somewhat arbitrary.
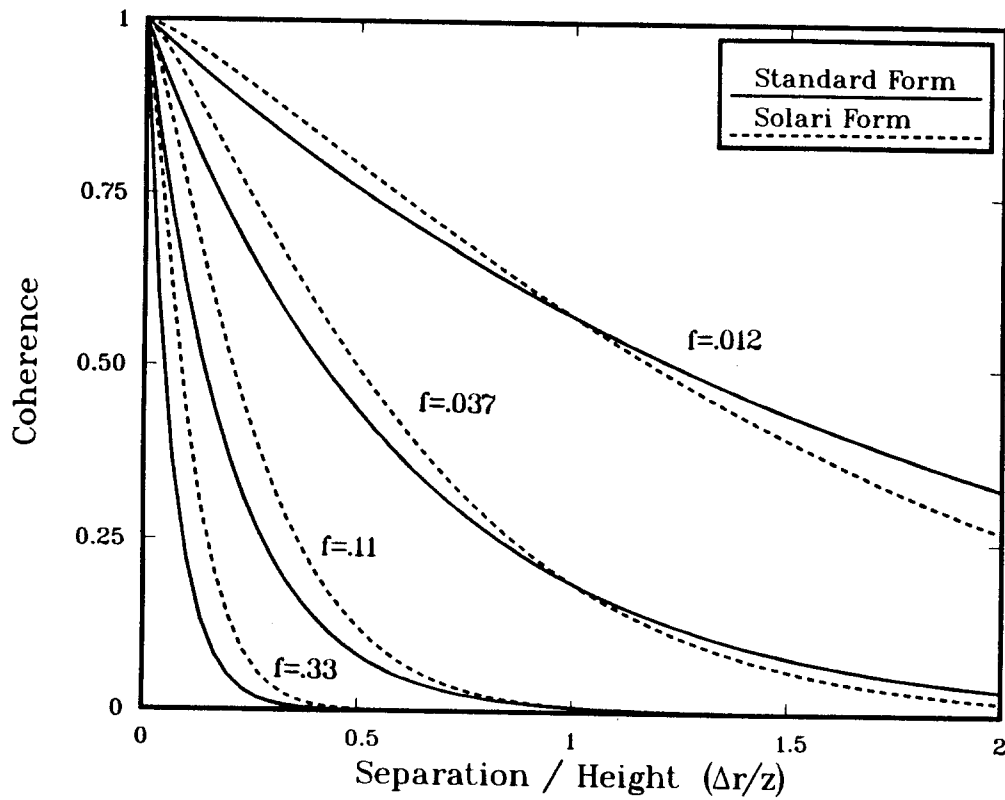
Figure 4.1. The coherence function is plotted as a function of spatial separation evaluated at four frequencies ($f = .012$, $.037$, $.11$, and $.33$ Hz). The solid lines are the standard exponential form and the dashed lines are Solari's suggested form (with $U = 8$m/s, $b = 12$, and $z = 30$m).

5. Rotational Sampling

The term *rotational sampling* was born out of an experiment in which anemometers were arranged around a circle in a vertical plane perpendicular to the mean wind direction. Wind speeds were then sampled successively from each anemometer to form a composite time series made up of wind speeds as seen by a rotating HAWT blade [14]. Experiments were later conducted with an anemometer on a rotating boom and with a Lidar scanner (laser anemometer). Rotational sampling is one method of checking simulations of spatially distributed turbulence. Unlike the PSD observed at a stationary point, the rotational PSD has peaks at the integer multiples of the rotating frequency. [1]

Rotational sampling with the Sandia method is accomplished by selecting wind speeds out of the full field at points in space and time that correspond to positions of a rotating HAWT blade. A rotationally sampled PSD can then be estimated from the sampled time series with the aid of a Fourier transform.

Simulation techniques have been devised by Pacific Northwest Laboratory (PNL) to generate the wind speeds for a point on rotating HAWT [14] and VAWT [15] blades. The PNL method analytically derives a rotationally sampled PSD and then uses the inverse Fourier transform to produce a time series. The major shortcoming of this method is that it can only simulate the wind speed at a single point on one turbine blade, while structural response is sensitive to the distribution of wind speed over the entire blade. The Sandia method, by simulating the wind speed at many points in space for all time steps and then sampling at the moving position of the turbine blade, can provide wind speed at many points on several blades. The disadvantage is that wind speeds are also generated at points in space and time that the blades will never occupy. The cost of obtaining wind speed at many points along the blades is therefore a large increase in the required storage space for simulation program execution.

The validity of rotational sampling with the Sandia method has recently been questioned in a PNL report by Powell and Connell [11]. In comparisons with measured rotationally sampled wind speeds and with empirically adjusted theoretical results [16], the Sandia method was claimed to be *less accurate*. No explanation for the differences was reported.

---

[1]Integer multiples of the rotating frequency are abbreviated as *per rev* frequencies — i.e., 1 per rev (1P) is the rotational frequency; 2 per rev (2P) is twice the rotational frequency, etc...

The reasons for the reported deficiency, which will be explained below, are listed here in order of decreasing importance:

1. Statistical variations in per rev spectral content were not accounted for in the PNL report.

2. Different input turbulence PSDs were used in the two approaches reported by PNL.

3. The exponential form of the coherence function previously suggested in the literature and used in the Sandia method is incapable of matching the measured rotationally sampled PSDs at all per rev frequencies.

4. An error in the code supplied by Sandia to PNL decreased the input coherence decrement by a factor of two.

The discrepancy is not due to any fundamental flaw in the Sandia method, as will be shown below. By using input turbulence and coherence models based on the recent synthesis of wind data by Solari [13], a better fit to the measured results can be obtained using the Sandia method than from other rotational sampling methods without losing the ability to generate wind speed at several points on the turbine blades.

To illustrate the effects of changes in turbulence PSD and coherence, simulations using the Sandia method, with various spectral and coherence inputs, are compared to the test case of Ref. 11. Rotational sampling is done about a circle with a 20m radius centered 30m above the ground at a rotational speed of (2/3)Hz. The sampling interval is 0.125sec (12 points per revolution) and the record length is 1024 points (128sec). The mean wind speed is 8m/s and the surface roughness coefficient (z_0) is 0.01m.

Table 5.1 lists the total variance of the turbulence and the distribution of variance in the per rev peaks for the *exact* PNL results (from Ref. 11) and for several different inputs to the Sandia method. The *exact* results are the PNL method results adjusted by empirical corrections that make the per rev variances agree with measured data [16]. Variances are listed in units of meters per second squared and (in parenthesis) normalized by the *exact* results, which are listed in the first line of the table. (The *exact* total variance was not published.) The results flagged with an * are from Powell and Connell [11].

The Sandia method results reported by PNL in Ref. 11, using both the Frost and Kaimal PSDs, have far from the desired distribution of variance, especially at one per rev (1P), as can be seen in Table 5.1. The SNL estimates using the Sandia

12

Table 5.1. The Distribution of variance over the per rev harmonics are shown for the PNL method (first two rows) and for the Sandia method using various PSD and coherence models. Variance is in units of $(m/s)^2$; the numbers in parentheses are the per rev variances normalized by the *exact* (corrected) values given in the first row.

PSD Model	Coherence Model	Coh. Dec. C	Total Variance	Per Rev Variance				
				1P	2P	3P	4P	5P
Exact (corrected) PNL Results*		—		.263	.097	.054	.038	.033
Uncorrected PNL Results*			.837	.359	.111	.055	.034	.024
				(1.37)	(1.14)	(1.02)	(0.90)	(0.73)
Frost* (PNL)	Standard	3.75	1.10	.152	.089	.060	.052	.047
				(0.58)	(0.92)	(1.11)	(1.38)	(1.42)
Frost (SNL)	Standard	3.75	1.17	.201	.090	.058	.045	.041
				(0.76)	(0.93)	(1.07)	(1.19)	(1.24)
Kaimal* (PNL)	Standard	10.0	.532	.086	.065	.044	.043	.040
				(0.33)	(0.67)	(0.82)	(1.14)	(1.21)
Kaimal (SNL)	Standard	10.0	.607	.129	.070	.049	.040	.038
				(0.49)	(0.72)	(0.91)	(1.06)	(1.15)
von Karman (SNL)	Standard	12.0	.776	.171	.085	.059	.048	.042
				(0.65)	(0.88)	(1.09)	(1.27)	(1.27)
Solari ($\beta = 7.5$)	Standard	12.0	1.00	.215	.104	.069	.055	.048
				(0.82)	(1.07)	(1.28)	(1.46)	(1.45)
Solari ($\beta = 7.5$)	$(\Delta r/z_m)^{0.25}$	12.0	1.00	.237	.105	.064	.047	.039
				(0.90)	(1.08)	(1.19)	(1.25)	(1.18)
Solari (Random β)	$(\Delta r/z_m)^{0.25}$	Random	1.04	.239	.111	.069	.053	.045
				(0.91)	(1.14)	(1.28)	(1.41)	(1.36)
Solari (Random β)	$(\Delta r/z_m)^{0.50}$	Random	1.04	.259	.111	.064	.046	.038
				(0.98)	(1.14)	(1.19)	(1.22)	(1.15)
Solari	$(\Delta r/z_m)^{0.25}$	Random	1.09	.237	.098	.057	.041	.033
Simulating one sample per rev				(0.90)	(1.01)	(1.06)	(1.09)	(1.00)
* Results taken from Powell and Connell, Ref. 11.								

method with the Frost and Kaimal PSDs are substantially better. The only apparent difference is that PNL used only one record (125 seconds long) to estimate the rotationally sampled PSD, while the SNL results are the ensemble average of 100 records. The variability in per rev variance from record to record is surprisingly large; the coefficient of variation (standard deviation divided by the mean) is about 0.2 for the higher per revs and 0.25 at one per rev. It is therefore likely that most of the difference is due to PNL's failure to account for statistical variations in the per rev variances.

The von Karman PSD has slightly more low frequency variance than the Kaimal PSD (see Fig. 3.1), which is reflected in a higher total rotationally sampled variance, and a better fit to the *exact* results. The von Karman PSD is consistent with the PNL method for estimating rotationally sampled PSDs. This is another reason that the PNL method results, which are based on the von Karman PSD, did not match the Sandia method results, which had been based on the Kaimal PSD, in Ref. 11.

The Solari PSD is about the same as the Kaimal PSD when the random parameter β is at its minimum value of 5, and has more low frequency variance when β is high (see Fig. 3.2). Table 5.1 shows the rotationally sampled per rev variances for the Solari PSD with β fixed at the mean value ($\beta = 7.5$) and with the same exponential form of the coherence as used in all the above results. The one per rev variance is still too low and the higher per rev variances are too high. Augmenting the coherence by $(\Delta r/z_m)^{0.25}$, as Solari suggests, makes a substantial improvement on the match between simulated and *exact* results. Randomizing the parameters β and C has a minor influence on the results. Because augmenting by $(\Delta r/z_m)^{0.25}$ fills the need to increase the coherence at small separations and increase it at large separations, while the choice of 0.25 appears somewhat arbitrary, a power of 0.50 was also tried, resulting in an improved fit to the *exact* results (see Table 5.1).

The results in Table 5.1 indicate that a wide variety of rotationally sampled PSDs can be obtained with the Sandia method depending on the input models of turbulence PSD and coherence. The Solari models produce a good fit to the *exact* results, better than the uncorrected PNL method. An even better fit is possible by using $(\Delta r/z_m)^{0.50}$ instead of $(\Delta r/z_m)^{0.25}$ in the coherence model. However, a better fit for this one application may not be a sufficient reason to override Solari's choice of 0.25. It is also not clear that the goal should be to match the *exact* results precisely. There is a great deal of variability in per rev variance in any given wind sample; even the *exact* results may not be perfectly representative.

6. Efficient Simulation for HAWT Applications

In HAWT applications the wind speed is simulated at points arranged around the circular path followed by the blades. With the method described above, the time series at each point is simulated at a rate of the number of points per revolution, N_{pr}, times the rotating frequency in Hertz, Ω (i.e., $\Delta t = 1/N_{pr}\Omega$). The time series at each point is only sampled once per revolution by each blade, making the sampling rate equal to the number of blades, N_b, times Ω. Because N_{pr} is always much greater than N_b, most of the data is wasted. It is therefore more efficient to simulate data at each point at a rate of $N_b\Omega$ with the time of the samples shifted to correspond to the time of blade passage.

The trick is to make each simulated data point correspond to the exact time that the wind turbine blade occupies that point in space. For evenly spaced points around a circle and constant rotational speed, there must be an equal time lag between simulations at each point. The time lag is implemented by shifting the phase of each frequency component in the PSD by the appropriate amount before transforming into the time domain.

The method may be illustrated by taking the specific example in **Fig. 6.1**, which has $N_{pr} = 12$, $N_b = 2$, and only one radial set of points ($N = N_{pr}$). The N_{pr} points are divided into N_b groups with a location index, l_j, ranging from 0 to $(N_{pr}/N_b) - 1$ in each group. The blades are initially located at the $l_j = 0$ points.

Simulating as above at a frequency of $N_b\Omega$ will produce one wind speed value at each point in space every time the blades are at the $l_j = 0$ locations. The wind speed at the $l_j > 0$ points must be lagged in time to correspond to the time of blade passage. The time lag is implemented by applying a phase shift, ϕ_{jm}, that depends on the location index, l_j, and the frequency component, f_m.
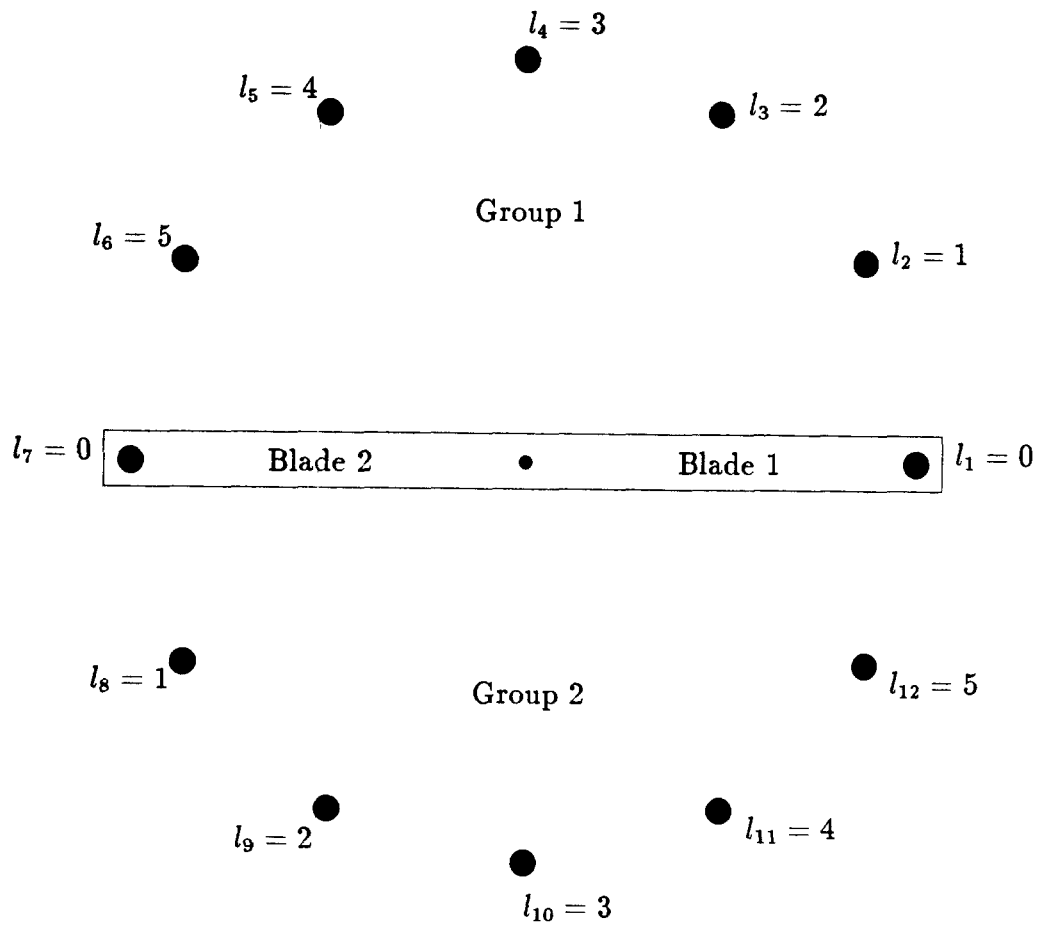
$$\phi_{jm} = l_j \left(\frac{2\pi}{N_{pr}} \right) \left(\frac{f_m}{\Omega} \right) \tag{6.1}$$

Equation 2.6 then becomes

$$V_j(f_m) = \sum_{k=1}^{j} H_{jk}(f_m) e^{i(\theta_{km} - \phi_{jm})} \tag{6.2}$$

The time domain representation is again obtained by taking the inverse Fourier transform of **V**. The odd samples (1,3,5,...) in the Group 1 time series belong to

15

Figure 6.1. Example of the locations of points for wind simulation with application to HAWTs.

$l_4 = 3$

$l_5 = 4$

$l_3 = 2$

Group 1

$l_6 = 5$

$l_2 = 1$

$l_7 = 0$ Blade 2   •   Blade 1 $l_1 = 0$

$l_8 = 1$

Group 2
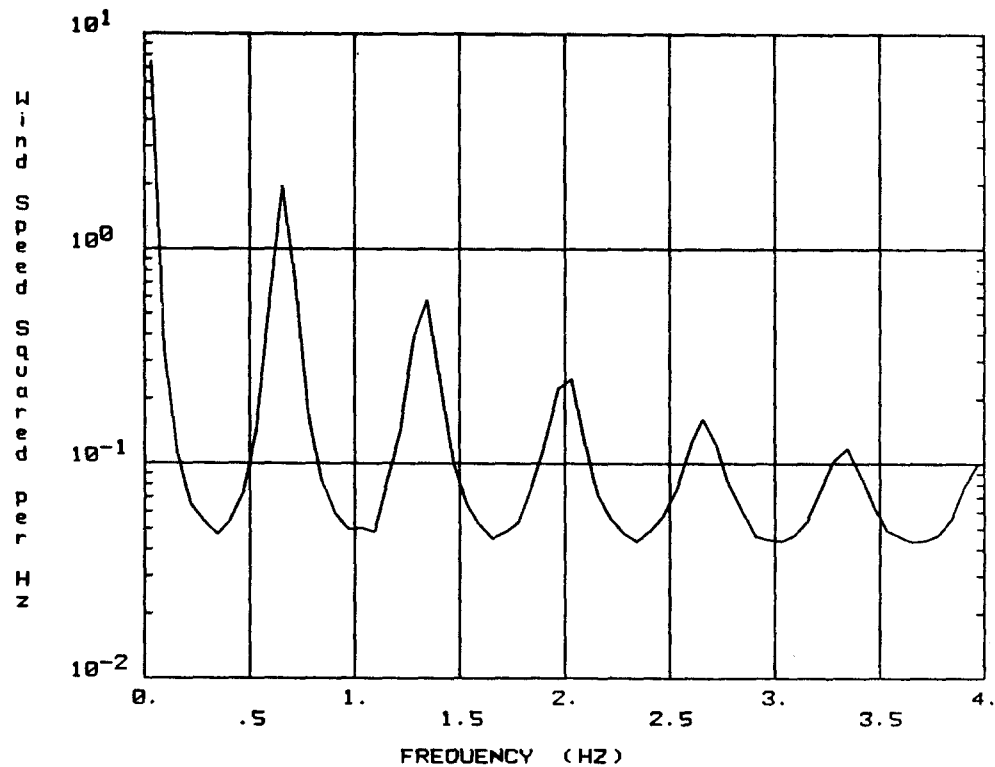
$l_{12} = 5$

$l_9 = 2$

$l_{11} = 4$

$l_{10} = 3$

Figure 6.2. Rotationally sampled PSD based on the Solari PSD and coherence using the full field Sandia method.

Blade 1 and the even samples belong to Blade 2. The reverse is true of the Group 2 time series. Every data sample in the time series of every point is therefore sampled by one of the blades so there are no longer any *spurious* data. The reduction in storage requirements and computation time is a factor of N_{pr}/N_b.

The rotationally sampled PSD with the full field approach using the Solari model for turbulence and coherence (with random parameters) is shown in Fig. 6.2. The PSD estimated with the *one sample per rev* method (simulating wind for only one blade) is shown in Fig. 6.3. The integrated per rev variance is about the same at 1P and is slightly reduced (about 15%) at higher per revs, as shown in Table 5.1. The per rev variance from the one sample per rev method is within 10% of the *exact* results for the first five per revs — a better fit than any other known method.

The greatest difference between simulating the full field and only simulating those data points that will be sampled is the minimum level of the PSD. Figure 6.2 shows a minimum level of PSD content at about .05 $(m/s)^2/Hz$, while the one sample per rev PSD has minima around .02 $(m/s)^2/Hz$. This *background* level comes from the high frequency portion of the input turbulence where the coherence is very small
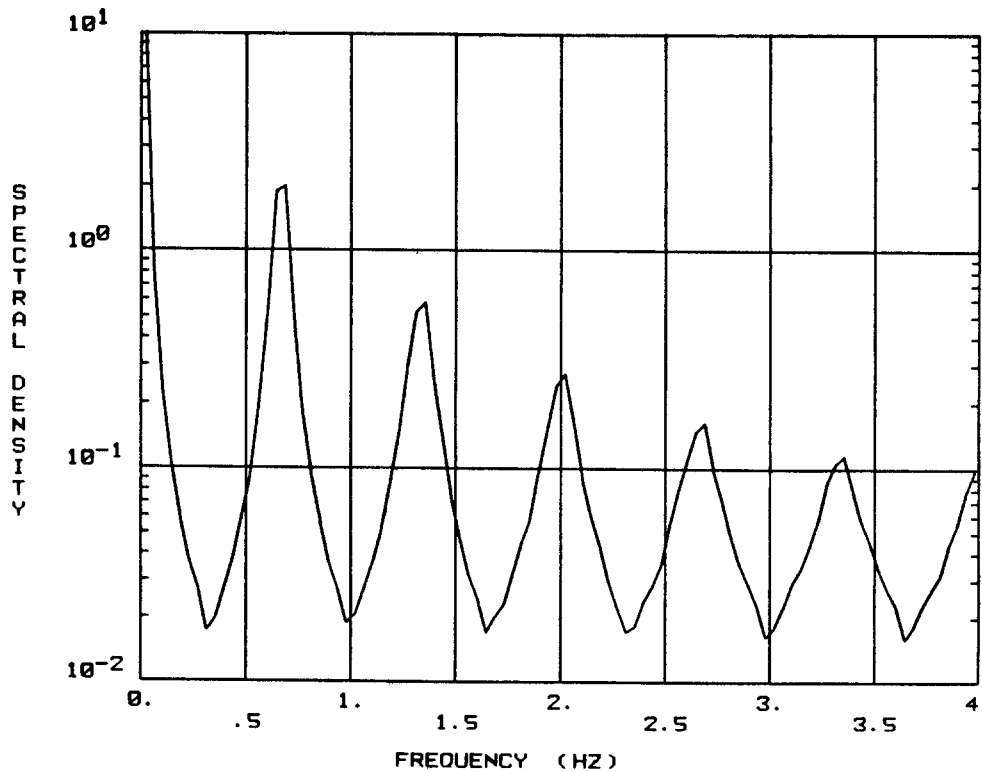
17

Figure 6.3. Rotationally sampled PSD based on the Solari PSD and coherence simulating one sample per revolution for each input point.

(see Eq. 4.1 and Fig. 4.1). The high frequency input is therefore nearly uncorrelated, even at closely spaced points, and shows up as a white-noise background on the rotational PSD. The one sample per rev method has a maximum frequency (Nyquist frequency) of one half per rev ($\Omega/2$) so the white background is omitted. The full field method exhibits a similar decrease in the minimum when the spectral content at frequencies above $\Omega/2$ is set to zero, as shown in Fig. 6.4.

The improved fit to the *exact* per rev variances when simulating only one point per rev is due to the elimination of the background, uncorrelated, high-frequency input. It is not clear that this is desirable, because the *exact* results could also be suffering from a lack of high-frequency input, which could even occur in measurements (i.e., due to insufficient anemometer frequency response). The full field method includes all of these high frequencies and may therefore be more accurate. The uncorrelated input could be added to the one sample per rev simulation by simply adding white noise with variance equal to the spectral content of the turbulence above a frequency of $\Omega/2$. When simulating wind speeds for N_B blades, the missing spectral content is above $N_B\Omega/2$.
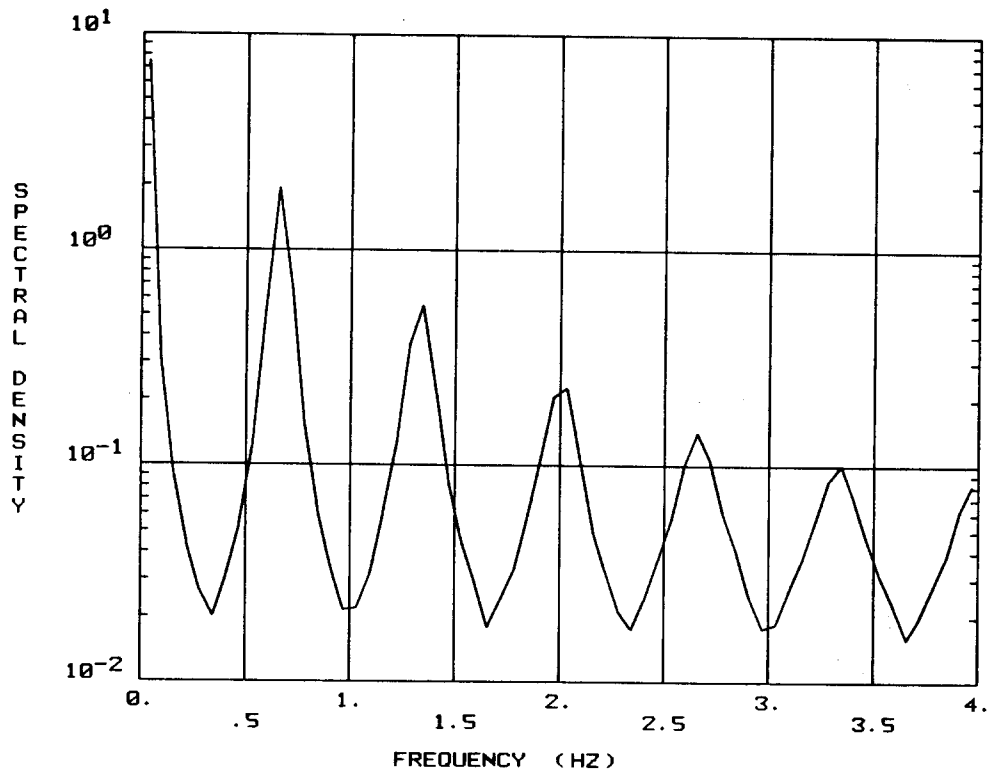
18

Figure 6.4. Rotationally sampled PSD based on the Solari PSD and coherence
using the full field Sandia method with the turbulence PSD set to zero
at frequencies above one half per rev ($\Omega/2$).

The structural implications of the missing spectral content between per rev fre-
quencies is not obvious for two reasons: (1) The *aerodynamic loads* on the blades are
nonlinearly related to the incident wind speed, and (2) the blades may not respond
aerodynamically to fluctuations of such high frequency and small scale. The per rev
spectral content is between 2 times (at 5P) and 40 times (at 1p) greater than the
background level (see Fig. 6.2) and is therefore the most important part of the PSD
to match.

7. Spatial Interpolation

The efficient simulation for HAWT applications in the previous section can not be used for VAWT applications because of the looping paths that VAWT blades trace out in the moving field of turbulence. It is therefore necessary to minimize the number of input points over the swept area of the wind turbine and interpolate wind speed values between those points. For example, a 4x4 rectangular grid of 16 points was used to cover the swept area of the 25 meter diameter VAWT in Ref. 6. Obtaining wind speed values at locations in space lying between simulation points can result in a loss of variance due to the averaging inherent in interpolation. Simulating wind speed for arbitrary locations on a moving VAWT blade therefore requires that this lost variance be replaced before the aerodynamic loads are calculated.

The wind speed, Y, at a location not at a grid point can be estimated by an interpolated value, $\tilde{Y}$, by taking a weighted sum of the n surrounding simulated values, Y_j;

$$\tilde{Y} = \sum_{j=1}^{n} W_j Y_j \tag{7.1}$$

The variance of $\tilde{Y}$ is the expected value of $\tilde{Y}^2$ (assuming a zero mean), given by

$$E[\tilde{Y}^2] = \sum_{j=1}^{n} \sum_{k=1}^{n} W_j W_k E[Y_j Y_k] \tag{7.2}$$

The actual variance of Y, $E[Y^2]$, may be known a priori, or may be interpolated from the grid points by the same scheme as given in Eq. 7.1.

If Y_j and Y_k are perfectly correlated (and have the same variance), then $E[Y_j Y_k] = E[Y_j^2] = E[Y_k^2]$ and there is no loss of variance. However, there will usually be some difference in variance and lack of correlation in wind speed reflected in the coherence function and quantified by the cross spectral density, G_{jk}. (See also Eq. 2.1 and recall that because $G_{jk}(f)$ is real valued, $\int_0^\infty G_{jk}(f)df = E[Y_j Y_k]$.) The normalized error is the missing variance divided by the correct variance, $E[Y^2]$, and can therefore be expressed as

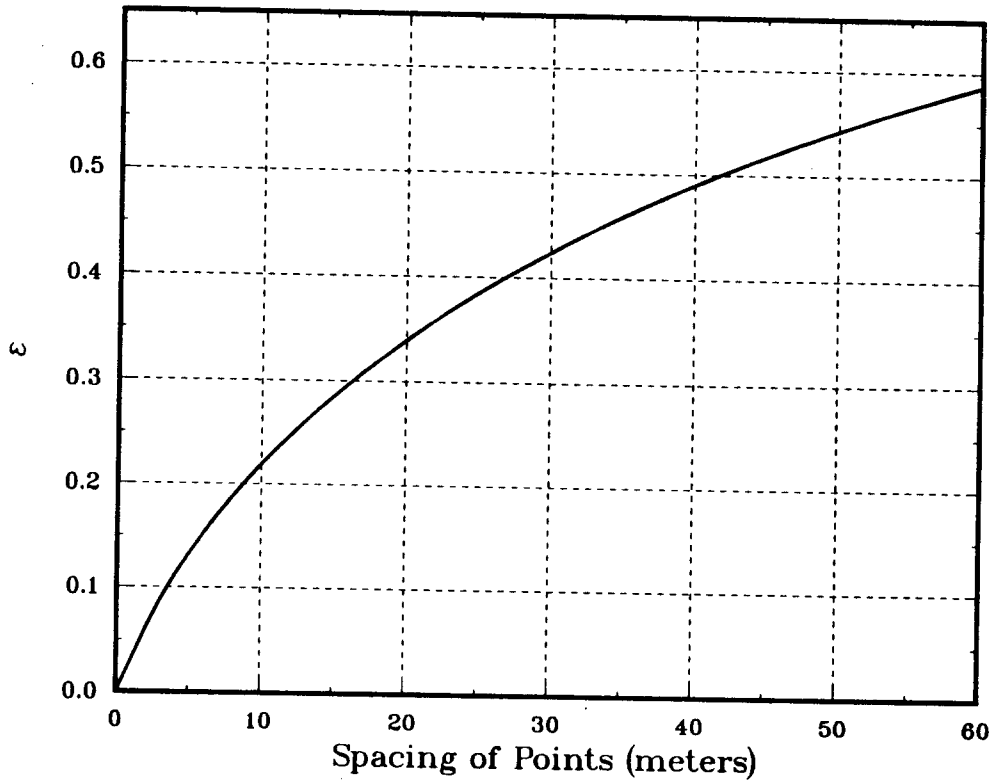$$Error = 1 - \frac{\sum_{j=1}^{n} \sum_{k=1}^{n} W_j W_k \int_0^\infty G_{jk}(f)df}{E[Y^2]} \tag{7.3}$$

20

Figure 7.1. Potential loss of variance, ϵ, as a function of the distance between
points for interpolating wind speed (using Solari's PSD and coherence).

The potential loss of variance for each pair of points can be expressed by defining
the parameter ϵ_{jk},

$$\epsilon_{jk} = 1 - \frac{\int_0^\infty G_{jk}(f)df}{E[Y^2]} \qquad (7.4)$$

The potential (or maximum) loss of variance, ϵ_{jk}, is therefore a function of the
level of correlation between points j and k, which is in turn a function of the distance
between the points, Δr. The value of ϵ_{jk} is plotted as a function of the point spacing
in Fig. 7.1 (using the Solari PSD and coherence with average values for the random
parameters). This potential for loss of variance is also the integrated difference
between the PSD and the CSD of any two points, if the points have identical PSDs.
Figure 7.2 shows how ϵ_{jk} is distributed over frequency in this case by plotting the
turbulence CSDs for point spacings of 10, 20, and 30 meters. The actual PSD of
the interpolated data will lie between the CSD and the "Original PSD," shown in
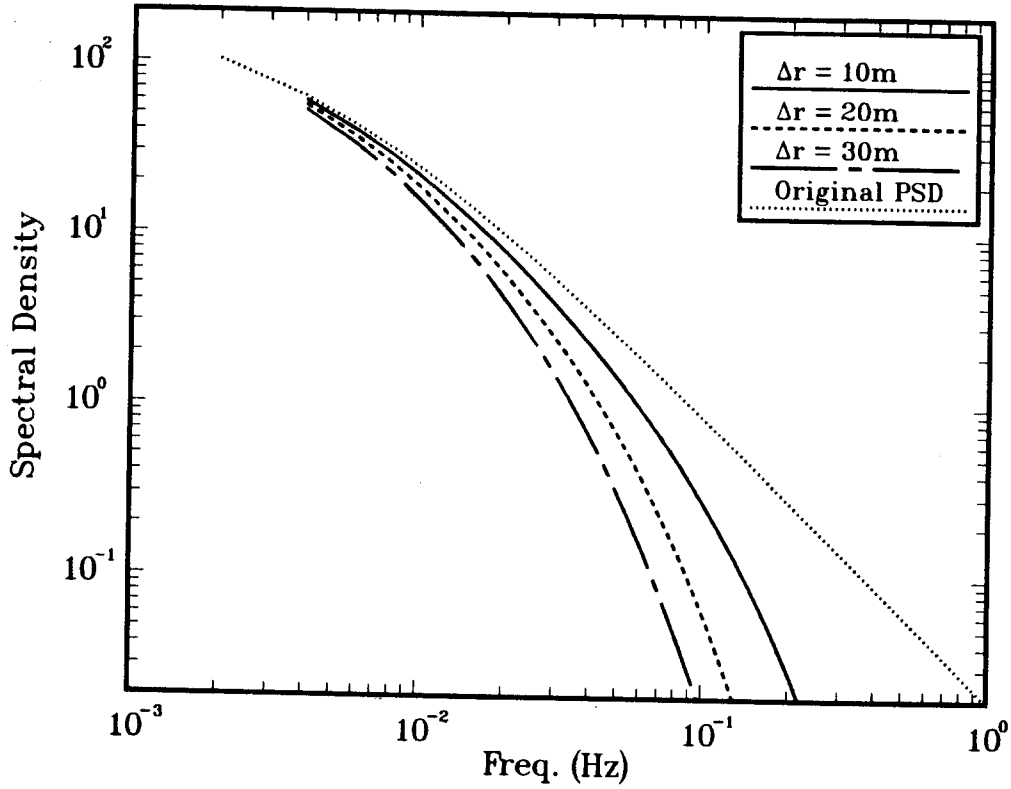Fig. 7.2.

21

Figure 7.2. CSDs of turbulence for points with 10, 20, and 30 meter spacings compared with the PSD at each point (Original PSD).

The normalized error is the fraction of ϵ_{jk} actually lost, as shown by substituting Eq. 7.4 into Eq. 7.3.

$$Error = 1 - \sum_{j=1}^{n} \sum_{k=1}^{n} W_j W_k (1 - \epsilon_{jk}) \qquad (7.5)$$

Using the fact that $\epsilon_{jj} = 0$ and assuming the interpolation weights have the usual property that

$$\sum_{j=1}^{n} \sum_{k=1}^{n} W_j W_k = 1$$

the expression for the error can be reduced to

$$Error = 2 \sum_{j=1}^{n-1} \sum_{k=j+1}^{n} W_j W_k \, \epsilon_{jk} \qquad (7.6)$$

22
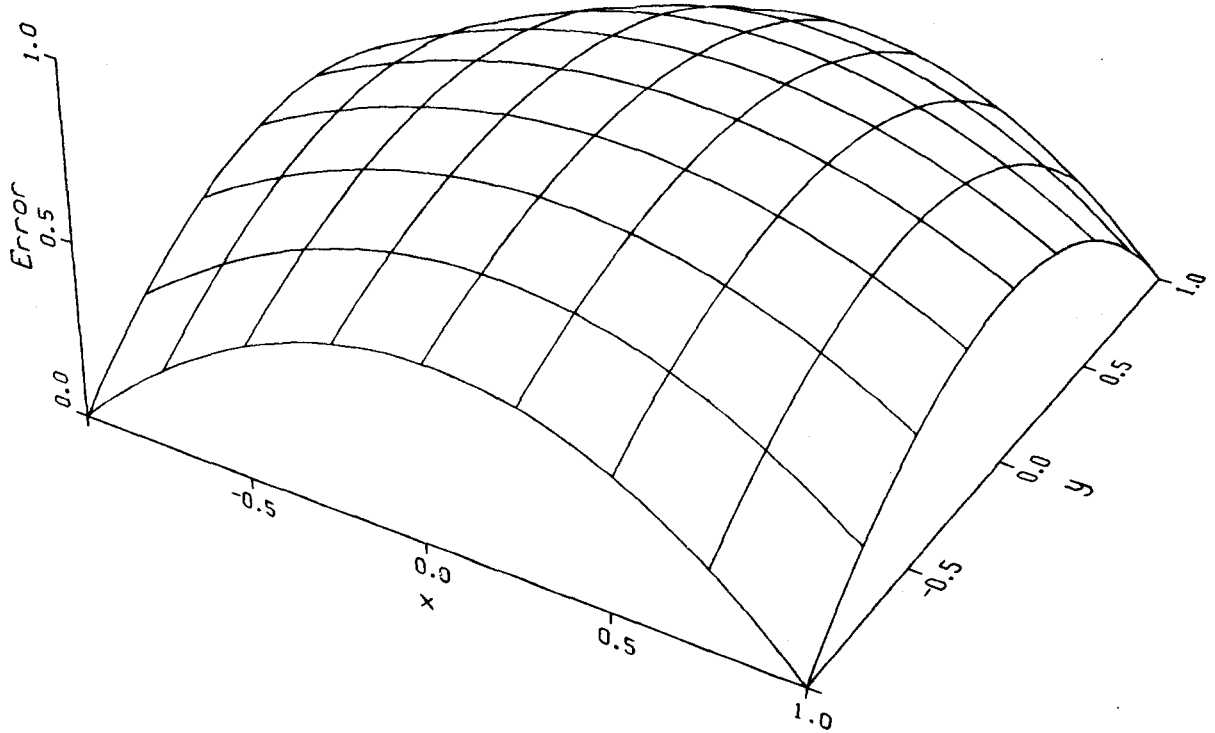
Figure 7.3.   Distribution in error (loss of variance), as a fraction of ϵ, for bilinear interpolation over a square region.

The error therefore depends on the weights used in the interpolation scheme.

For example, consider a square region to be interpolated from the four corner values with a bilinear interpolation. Let $\epsilon = \epsilon_{jk}$, where j and k are adjacent corners, be the characteristic potential loss of variance for the region. Figure 7.3 shows approximately how the error, as a fraction of ϵ, will be distributed over the region. There will be no loss of variance at each corner. The maximum error, about $3\epsilon/4$, is at the center. The error at the center of each side is $\epsilon/2$.

The lost variance represents the portion of the process that is uncorrelated between adjacent simulation points. To simulate a time series at some location inside the region, an interpolated time series could first be generated from the corner points. The missing part could be simulated *independently* by taking an inverse Fourier transform of a weighted sum of the differences between the PSDs and CSDs in Fig. 7.2 (replace ϵ_{jk} with the (PSD - CSD) for each pair of points in Eq. 7.6). The two time series could then be added together to obtain a result with the correct variance.

For VAWT applications, however, complete time series at intermediate locations

are not needed, only samples of time series at intermediate locations are needed. Each wind speed sample on the moving blade is taken from a different location in space where the missing high frequency variance (see Fig. 7.2) is relatively uncorrelated. The missing variance can therefore be replaced by adding uncorrelated Gaussian increments (white noise) to the wind speed samples, where the variance of the added increment is equal to the missing part at that location in space. The effect is the same as in the previous section where there is missing high frequency content when only N_B points per revolution of a HAWT are simulated. In both cases, the missing frequency content is well approximated by white noise when applied to a blade moving through the turbulence field.

There are two cases in which the white noise approximation may be in error: (1) where the blade is moving slowly (near the attachments to the tower), and (2) when simulating at very closely spaced points on the blade. In case (1), the error may be neglected because points where the blade is moving slowly are also points where the aerodynamic loads are small. In case (2), there is potential for slightly underestimating the contribution of the resulting aerodynamic loads to the lower modes of the structure. Care must be taken to avoid refining the spacing of locations at which loads are calculated beyond the level at which the winds can be accurately simulated. Similarly, too small an interval in blade azimuth position can cause case (1) type errors, even at the equator. A practical limit on the spacing of points on the blade would be the distance that the blade equator travels between time steps.

8. Conclusions

1. The Sandia method for three-dimensional turbulence simulation is capable of matching the best estimates of rotationally sampled PSDs better than any other simulation method currently available. The input models of turbulence PSD and coherence are what determine the accuracy of the method (see Table 5.1).

2. Models for atmospheric turbulence PSD and coherence with coefficients that are modeled as random variables (Eqs. 3.4, 4.1, and 4.2) provide good results for rotational sampling. The recent paper by Solari [13] provides estimates of the distributions of these coefficients.

3. A coherence that is exponential in Δr, as previously assumed, is not capable of matching the suggested distribution of variance in rotationally sampled PSDs. Solari's suggestion of augmenting by $(\Delta r / z_m)^{0.25}$ is a definite improvement; simulations using $(\Delta r / z_m)^{0.50}$ give even better results for this one test case. It is recommended that Solari's suggestion (Eq. 4.2) be followed.

4. An improvement to the Sandia method for full field wind simulation permits simulation of only those samples that are actually used in rotational sampling. This reduces the storage requirement and computation time by a factor of the number of divisions per rev divided by the number of blades. The match between published rotationally sampled PSDs and the simulation results is excellent (see Table 5.1). This improvement is useful for HAWT analysis, but not for VAWT analysis.

5. When interpolating simulated wind speeds, there will be a reduction in variance of the interpolated data. The error is quantified in terms of the cross spectral density functions, permitting an estimate of the missing variance at any location in space. Because the missing part is uncorrelated over the region of the interpolation, simulations of wind speed at a point on a rotating VAWT blade can be generated by adding uncorrelated Gaussian variates, with the appropriate variance for each location, to the interpolated values.

9. References

1. Veers, P.S., "Modeling Stochastic Wind Loads on Vertical Axis Wind Turbines," SAND83-1909, Sandia National Laboratories, Albuquerque, NM, September, 1984.

2. Homicz, G.F., "VAWT Stochastic Loads Produced by Atmospheric Turbulence," SAND87-1256C, Sandia National Laboratories, Albuquerque, NM, presented at: 7th *ASME Wind Energy Symposium*, New Orleans, LA, January 10-14, 1988.

3. Lobitz, D.W., "NASTRAN-based Software for the Structural Analysis of Vertical and Horizontal Axis Wind Turbines," Proceedings, *European Wind Energy Conference*, Hamburg, F.R. Germany, October 22-26, 1984, ed. W. Palz, *Commission of the European Communities*, Published by H.S. Stephens and Associates, Bedford, England, 1985.

4. Oscar, D.S. and T.L. Paez, "Analysis of Wind Turbines on Offshore Support Structures Excited by Random Wind and Random Waves," Proceedings, 7th *ASME Wind Energy Symposium*, New Orleans, LA, January 10-14, 1988.

5. Anderson, M.B., S.J.R. Powles, and E.A. Bossanyi, "The Response of a Vertical Axis Wind Turbine to Fluctuating Aerodynamic Loads," Proceedings, 7th *British Wind Energy Association Conference*, Oxford University, March 27-29, 1985.

6. *Vertical Axis Wind Turbine Turbulent Wind Response Model, Volume I*, prepared by Indal Technologies Inc. on behalf of Sandia National Laboratories, Albuquerque, NM, Document No. 32-3044, February, 1987.

7. Shinozuka, M. and C.-M. Jan, "Digital Simulation of Random Processes and Its Applications," *Journal of Sound and Vibration*, Vol. 25, No. 1, pp. 111-128, 1972.

8. Smallwood, D.O., "Random Vibration Testing of a Single Test Item with a Multiple Input Control System," Proceedings, *Institute of Environmental Sciences*, April, 1982.

9. von Karman, T. "Progress in the Statistical Theory of Turbulence," *Proceedings of the National Academy of Science*, Vol. 34, 1948.

10. Frost, W., B.H. Long, and R.E. Turner, "Engineering Handbook on the Atmospheric Environmental Guidelines for Use in Wind Turbine Development," NASA Technical Paper 1359, December, 1978.

11. Powell, D.C. and J.R. Connell, "Review of Wind Simulation Methods for Horizontal-Axis Wind Turbine Analysis," PNL–5903, Battelle Pacific Northwest Laboratory, Richland, WA, June, 1986.

12. Kaimal, J.C., J.C. Wyngaard, Y. Izumi, and O.R. Cote, "Spectral Characteristics of Surface-Layer Turbulence," *Quarterly Journal of the Royal Meteorological Society*, 98, 1972.

13. Solari, G., "Turbulence Modeling for Gust Loading," *ASCE Journal of Structural Engineering*, Vol. 113, No. 7, July, 1987.

14. Connell, J.R., "The Spectrum of Wind Speed Fluctuations Encountered by a Rotating Blade of a Wind Energy Conversion System," PNL–4083, Battelle Pacific Northwest Laboratory, Richland, WA, November, 1981.

15. George, R.L., "Simulation of Winds as Seen by a Rotating Vertical Axis Wind Turbine Blade," PNL–4914, Battelle Pacific Northwest Laboratory, Richland, WA, February, 1984.

16. Powell, D.C., J.R. Connell, and R.L. George, "Verification of Theoretically Computed Spectra for a Point Rotating in a Vertical Plane," PNL–5440, Battelle Pacific Northwest Laboratory, Richland, WA, 1985.

10. Appendix A — Simulation Example

To illustrate how correlated time series are constructed from uncorrelated inputs, consider an example where a single frequency component, f_m, is simulated at four points in space as shown in Fig. 10.1. The distances between points are

$$\Delta r_{12} = \Delta r_{13} = \Delta r_{24} = \Delta r_{34} = 1.0$$
$$\Delta r_{23} = 1.2$$
$$\Delta r_{14} = 1.6$$

For the sake of simplicity, let the coherence be exponential such that

$$Coh_{jk} = e^{-\Delta r_{jk}}$$

The coherences in this case are

$$Coh_{12} = Coh_{13} = Coh_{24} = Coh_{34} = 0.37$$
$$Coh_{23} = 0.30$$
$$Coh_{14} = 0.20$$

Let the PSDs at all four points be $G_{jj}(f_m) = 2/\Delta f$ such that the discrete representation is $S_{jj}(f_m) = G_{jj}(f_m)\Delta f/2 = 1.0$. The resulting spectral matrix is

$$\mathbf{S}(f_m) = \begin{bmatrix} 1.0 & .37 & .37 & .20 \\ .37 & 1.0 & .30 & .37 \\ .37 & .30 & 1.0 & .37 \\ .20 & .37 & .37 & 1.0 \end{bmatrix}$$

Solving for $\mathbf{H}$ using Eq. 2.3 yields

$$\mathbf{H}(f_m) = \begin{bmatrix} 1.0 & 0 & 0 & 0 \\ .37 & .929 & 0 & 0 \\ .37 & .176 & .912 & 0 \\ .20 & .319 & .263 & .888 \end{bmatrix}$$

The matrix of uncorrelated inputs is composed of the diagonal entries

$$X_{kk}(f_m) = e^{i\theta_{km}}$$

28

where the θ_{km} are uniformly distributed random variables on the interval from 0 to 2π. We can let θ_{1m} be zero and select the other three phases randomly without loss of generality.

$$\theta_{1m} = 0.0$$
$$\theta_{2m} = 0.80$$
$$\theta_{3m} = 5.79$$
$$\theta_{4m} = 3.58$$

The product $\mathbf{HX}$ then gives

$$\mathbf{H}(f_m)\,\mathbf{X}(f_m) = \begin{bmatrix} 1.0\,e^{0.0i} & 0 & 0 & 0 \\ .37\,e^{0.0i} & .929\,e^{0.80i} & 0 & 0 \\ .37\,e^{0.0i} & .176\,e^{0.80i} & .912\,e^{5.79i} & 0 \\ .20\,e^{0.0i} & .319\,e^{0.80i} & .263\,e^{5.79i} & .888\,e^{3.58i} \end{bmatrix}$$

Each entry in the vector $\mathbf{V}$ is the sum of a row of $\mathbf{HX}$.

$$V_{1m} = 1.0\,e^{0.0i}$$
$$V_{2m} = 1.216\,e^{0.58i}$$
$$V_{3m} = 1.332\,e^{6.05i}$$
$$V_{4m} = 0.312\,e^{5.22i}$$

Figure 10.2 is a phase plane plot of the random inputs for the mth frequency component in this example. Notice that the inputs are scattered over the entire phase plane. Figure 10.3 shows the resulting correlated outputs in phase space. The correlation between points has brought the output into closer phase alignment than the random inputs. If the correlation had been zero, the off-diagonal terms in $\mathbf{H}$ would be zero and the phases would have been unchanged. If the coherence had been unity, only the first column of $\mathbf{H}$ would have been nonzero and all of the output phases would have been equal to θ_{1m}. Values of coherence between zero and one enforce phase alignment at different levels of strictness. For example, points 1 and 2 had an input phase difference of 0.80 radians, but, due to the coherence of 0.37, that difference is reduced to 0.58 radians. The output phases are still random. (The selection of $\theta_{1m} = 0.0$ was done to simplify computations; in practice, θ_{1m} is a random variable just like the other phase angles.)

Notice that the output magnitudes at points 2, 3, and 4 are no longer exactly 1.0. The output magnitude depends on the relative phases of the random inputs. Over many points and frequency components, the variance will average near the specified level. In this example the average variance of the four outputs is only 9% greater than the specified level.

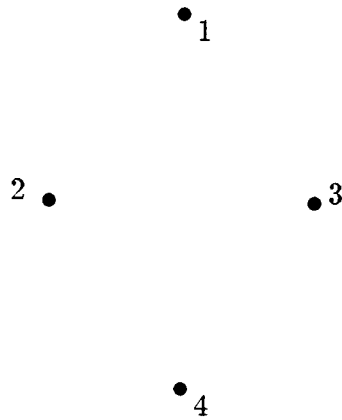Figure 10.1. Locations of points for the wind simulation example in Appendix A.

$\bullet$ 1

2 $\bullet$ $\bullet$ 3

$\bullet$ 4

Figure 10.2. Phase plane plot of the uncorrelated random inputs.

Im

X_{22}

X_{11} Re

X_{44} X_{33}
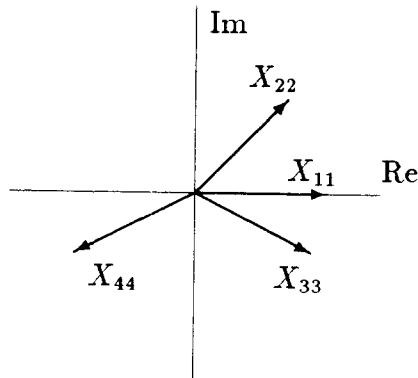
Figure 10.3. Phase plane plot of the correlated outputs.

Im

V_2

V_1 Re

V_4 V_3

J. B. Dragt
Nederlands Energy Research
  Foundation
(E.C.N.)
Physics Department
Westerduinweg 3 Petten(nh)
THE NETHERLANDS

Electric Power Research Inst.
3412 Hillview Avenue
Palo Alto, CA   94304
Attn: E. Demeo
        F. Goodman

Alcir de Faro Orlando
Pontificia Univer. Catolica
-PUC/Rj
Mechanical Engineering Dept.
R. Marques de S. Vicente 225
Rio de Janeiro, BRAZIL

Fayette Manufacturing Corp.
P.O. Box 1149
Tracy, CA   95378-1149
Attn: W. Thompson

FloWind Corporation (2)
1183 Quarry Lane
Pleasanton, CA   94566
Attn: L. Schienbein
        B. Im

A. D. Garrad
Garrad Hasson
10 Northampton Square
London EC1M 5PA
UNITED KINGDOM

H. Gerardin
Mechanical Engineering Dept.
Faculty of Sciences and
    Engineering
Universite Laval-Quebec
G1K 7P4
CANADA

dr. I. J. Graham
Southern University
Dept. of Mech. Engineering
P.O. Box 9445
Baton Rouge, LA 70813-9445

R. T. Griffiths
Univ. College of Swansea
Dept. of Mech. Engin.
Singleton Park
Swansea, SA2 8PP
UNITED KINGDOM

Indal Techn., Inc. (2)
3570 Hawkestone Road
Mississauga, Ontario
CANADA L5C 2V8
Attn: D. Malcolm
        C. Wood

Institut de Recherche
    d'Hydro-Quebec
1800, Montee Ste-Julie
Varennes, Quebec, JOL 2P.O.
CANADA
Attn: Bernard Masse

Iowa State University
Agricultural Engineering
Room 213
Ames, IA   50010
Attn: L. H. Soderholm

K. Jackson
West Wind Industries
P.O. Box 1705
Davis, CA   95617

R. E. Kelland
The College of Trades and
    Technology
P.O. Box 1693
Prince Philip Drive
St. John's, Newfoundland,
A1C 5P7   CANADA

Kinetics Group, Inc.
P.O. Box 1071
Mercer Island, WA   98040
Attn: J. Sladky, Jr.

KW Control Systems, Inc.
RD#4, Box 914C
South Plank Road
Middletown, NY   10940
Attn: R. H. Klein

Olle Ljungstrom
FFA, Aero. Research
Institute
Box 11021
S-16111 Bromma, SWEDEN

Robert Lynette
R. Lynette & Assoc., Inc.
15042 NE 40th Street
Suite 206
Redmond, WA 98052

Massachusetts Inst. of
  Technology
77 Massachusetts Avenue
Cambridge, MA   02139
Attn: Professor N. D. Ham
       W. L. Harris,
       Aero/Astro Dept.

US Wind Power (2)
160 Wheeler Road
Burlington, MA   01803
Attn: K. M. McNerney
       W. E. Holley

Michigan State University
Div. of Engin. Research
East Lansing, MI   48825
Attn: O. Krauss

Napier College of Commerce
   and Technology
Tutor Librarian, Tech. Fac.
Colinton Road
Edinburgh, EH10 5DT
ENGLAND

New Mexico Engineering
  Research Institute
UNM Campus P.O. Box 25
Albuquerque, NM   87131
Attn: G. G. Leigh

Ohio State University
Aeronautical & Astr. Dept
2070 Neil Avenue
Columbus, OH   43210
Attn: Prof. G. Gregorek

Oklahoma State University
Mech. Engineering Dept.
Stillwater, OK   76074
Attn: D. K. McLaughlin

Oregon State Univ. (2)
Mech. Engineering Dept.
Corvallis, OR   97331
Attn: R. E. Wilson
       Stel Walker

Ion Paraschivoiu
Depart. of Mech. Engineering
Ecole Polytecnique
CP 6079
Succursale A
Montreal H3C 3A7
CANADA

Jacques Plante
Hydro Quebec
Place Dupuis Ile etage
855 est rue Ste-Catherine
Montreal, Quebec
CANADA H2L 4P5

RANN, Inc.
260 Sheridan Ave., Suite 414
Palo Alto, CA   94306
Attn: A. J. Eggers, Jr.

Dr. R. Ganesh Rajagopalan
Aerospace Engineering Dept.
Iowa State University
404 Town Engineering Bldg.
Ames, IA   50011

Riso National Laboratory (3)
Postbox 49
DK-4000 Roskilde
DENMARK
Attn: Troels Friis Pedersen
       Helge Petersen
       Peter Hauge Madsen

Dr. Ing. Hans Ruscheweyh
Institut fur Leichbau
Technische Hochschule Aachen
Wullnerstrasse 7
FEDERAL REPUBLIC OF GERMANY

Beatrice de Saint Louvent
Establissement d'Etudes
  et de Recherches
  Meteorologigues
77 Rue de Serves
92106 Boulogne-Billancourt
Cedex, FRANCE

Gwen Schreiner
Librarian
National Atomic Museum
Albuquerque, NM 87185

Arnan Seginer
Professor of Aerodynamics
Technion-Israel Institute
  of Technology
Aeronautical Engin. Dept.
Haifa
ISRAEL

Farrell Smith Seiler, Editor
Wind Energy News Service
P.O. Box 4008
St. Johnsbury, VT 05819

David Sharpe
Dept. of Aeronautical Engin.
Queen Mary College
Mile End Road
London, E1 4NS
UNITED KINGDOM

Kent Smith
Instituto Tech. Costa Rico
Apartado 159 Cartago
COSTA RICA

Solar Energy Research Inst.
1617 Cole Boulevard
Golden, CO   80401
Attn: R. W. Thresher

Bent Sorenson
Roskilde Univ. Center
Energy Group, Bldg. 17.2
IMFUFA
P.O. Box 260
DK-400 Roskilde
DENMARK

Peter South
ADECON
32 Rivalda Road
Weston, Ontario, M9M 2M3
CANADA

G. Stacey
The University of Reading
Department of Engineering
Whiteknights, Reading,
RG6 2AY   ENGLAND

Dr. Derek Taylor
Alternative Energy Group
Walton Hall
Open University
Milton Keynes, MK7 6AA
UNITED KINGDOM

R. J. Templin
Low Speed Aerodynamics Lab.
NRC-National Aeronautical
  Establishment
Montreal Road
Ottawa, Ontario, K1A 0R6
CANADA

Texas Tech University
Mechanical Engineering Dept.
P.O. Box 4289
Lubbock, TX   79409
Attn: J. W. Oler

K. J. Touryan
Moriah Research
6200 Plateau Dr.
Englewood, CO   80111

Tulane University
Dept. of Mech. Engineering
New Orleans, LA   70018
Attn: R. G. Watts

United Engineers and
  Constructors, Inc.
P.O. Box 8223
Philadelphia, PA 19101
Attn: A. J. Karalis

Universal Data Systems
5000 Bradford Drive
Huntsville, AL   35805
Attn: C. W. Dodd

University of California
Institute of Geophysics
   and Planetary Physics
Riverside, CA   92521
Attn: Dr. P. J. Baum

University of Colorado
Dept. of Aerospace Engin.
   Sciences
Boulder, CO   80309
Attn: J. D. Fock, Jr.

Univ. of Massachusetts
Mechanical and Aerospace
   Engineering Dept.
Amherst, MA   01003
Attn: Dr. D. E. Cromack

University of Oklahoma
Aero Engineering Dept.
Norman, OK   73069
Attn: K. Bergey

University of Sherbrooke
Faculty of Applied Science
Sherbrooke, Quebec,
J1K 2R1 CANADA
Attn: A. Laneville
       P. Vittecoq

USDA, Agricultural Research
 Service
SW Great Plains Research Ctr.
Bushland, TX   79012
Attn: Dr. R. N. Clark

W. A. Vachon
W. A. Vachon & Associates
P.O. Box 149
Manchester, MA   01944

Dirk Vandenberghe
State Univ. of Ghent
St. Pietersniewstraat 41
9000 Ghent
BELGIUM

Washington and Lee Univ.
P.O. Box 735
Lexington, VA   24450
Attn: Dr. R. E. Akins

West Texas State Univ.
Govt. Depository Library
Number 613
Canyon, TX   79015

West Texas State Univ.
Department of Physics
P.O. Box 248
Canyon, TX   79016
Attn: V. Nelson

West Virginia University
Dept. of Aero Engineering
1062 Kountz Avenue
Morgantown, WV   26505
Attn: R. Walters

Wichita State University
Aero Engineering Dept. (2)
Wichita, KS   67208
Attn: M. Snyder
       W. Wentz

Wind Power Digest
P.O. Box 700
Bascom, OH   44809
Attn: Michael Evans

Giovanni Solari
Instituto di Scienza
   della Construzioni
University of Genova
Via Montallegro, 1
16145 Genova, ITALY

M. Shinozuka
Dept. of Civil Engin.
Columbia University
632 Mudd
New York, NY 10027

Steven R. Winterstein
Dept. of Civil Engin.
Stanford University
Stanford, CA   94305

C. Allin Cornell
110 Coquito Way
Portola Valley, CA 94025

Holt Ashley
Dept. Aero. & Astro. Eng.
Stanford University
Stanford, CA 94305

Michael B. Anderson
Sir Robert McAlpine & Sons, LTD
P.O. Box 74
London WC1N 1LG
UNITED KINGDOM

Mircea Grigoria
Dept of Civil Engr.
Cornell University
Ithica, NY 14853